

Impact of argon flow and pressure on the trapping behavior of nanoparticles inside a gas aggregation source

Jonas Drewes¹  | Suren Ali-Ogly²  | Thomas Strunskus¹  |
Oleksandr Polonskyi^{1,3}  | Hyněk Biederman²  | Franz Faupel¹  |
Alexander Vahl¹ 

¹Chair of Multicomponent Materials, Institute of Materials Science, Faculty of Engineering, Kiel University, Kiel, Germany

²Department of Macromolecular Physics, Charles University, Prague, Czech Republic

³Department of Chemical Engineering, Engineering II, University of California, Santa Barbara, California, USA

Correspondence

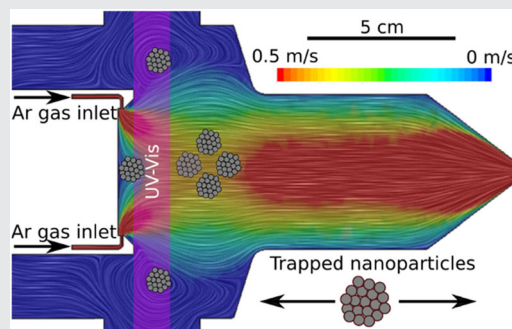
Alexander Vahl, Chair of Multicomponent Materials, Institute of Materials Science, Faculty of Engineering, Kaiserstraße 2, D-24143 Kiel, Germany. Email: alva@tf.uni-kiel.de

Funding information

Deutsche Forschungsgemeinschaft, Grant/Award Number: PO2299/1-1

Abstract

In this study, in situ UV–Vis spectroscopy is used to investigate the growth and transport of nanoparticles inside a gas aggregation source (GAS) dependent on the Ar gas flow and operating pressure. It was found that the nanoparticles were becoming trapped at different positions inside the GAS dependent on the gas flow. Moreover, in situ UV–Vis spectroscopy suggested the presence of large nanoparticles inside the GAS, which were not observed outside. Computational fluid dynamic simulations were performed to study the velocity distribution inside the GAS. Three distinct areas were identified, where nanoparticles can become trapped or lost. The gas flow velocity distribution was found to strongly impact the transport of nanoparticles.



KEYWORDS

computational fluid dynamic simulation, gas aggregation cluster source, gas-phase synthesis, in situ UV–Vis spectroscopy, sputter deposition

1 | INTRODUCTION

Metal nanoparticles (NPs) have received considerable attention over the last decades due to their unique properties in comparison to the properties of bulk metals,

resulting in high application potential in many fields like catalysis,^[1] photocatalysis,^[2–6] optics,^[7] resistive switching,^[8–15] and sensors.^[16–20] In particular, the optical properties of noble-metal NPs are highly interesting due to the presence of localized surface plasmons,^[21] and

Abbreviations: CFD, computational fluid dynamic; DLR, distal loss region; GAS, gas aggregation cluster source; LSPR, localized surface plasmon resonance; NPs, nanoparticles; PLR, proximal loss region; QCM, quartz crystal microbalance; SEM, scanning electron microscopy.

This is an open access article under the terms of the Creative Commons Attribution License, which permits use, distribution and reproduction in any medium, provided the original work is properly cited.

© 2021 The Authors. *Plasma Processes and Polymers* published by Wiley-VCH GmbH.

various applications are possible including molecular fluorescence,^[22] solar cells,^[23] and surface-enhanced Raman spectroscopy.^[24] Furthermore, molecularly labeled NPs that bond specifically to cancer cells were used for selective hyperthermia therapy of cancer cells without harming healthy cells.^[25] Another field of application for noble-metal NPs and especially silver NPs is antibacterial coatings for medicine, construction industry, clothing, and also food packaging.^[26] Here, their high surface-to-volume ratio enables fast ion release, which leads to tailored antibacterial properties.

There are several ways to produce metal NPs using either chemical, biological, or physical approaches. Chemical methods commonly use surfactants, which has the major disadvantage that the NPs created are contaminated by surfactant molecules.^[27] A physical vapor deposition approach to produce NPs is gas-phase synthesis in a “gas aggregation cluster source” (GAS). Many different kinds of GAS have been developed from the early 1970s based on for example, erosion techniques, effusive method, and supersonic jet expansion.^[28–30] In 1992, another physical vapor deposition method for the synthesis of NPs was proposed by Haberland et al.^[31] In this approach, a DC magnetron is used in a GAS, where the sputtered atoms condensate in the gas phase in the presence of inert gas. Henceforth, the abbreviation GAS always stands for a Haberland-type GAS.

In the GAS, the particle size can be tuned by various parameters, including the ratio of sputtering and cooling gases, the addition of molecular gases, the gas flow, the operating pressure in the aggregation volume, magnetron power, and the overall source geometry. All of these parameters influence the underlying processes of cluster formation from the nucleation up to the transport of NPs.^[32] Furthermore, it is commonly reported that the sizes of NPs synthesized with GAS can also be tuned by varying the aggregation length.^[33–36] This supports the common textbook understanding of the NP synthesis inside such GAS. It is known that after a stable nucleus is formed, it can grow while being transported toward the orifice by condensation of sputtered atoms or by coalescence with other nuclei or NPs.^[31,32,37] Regarding the transport of NPs inside the gas, it has been reported many times that the movement of NPs inside a GAS is caused by the drag force from the inert gas.^[31,35,38,39] Nevertheless, recent publications reported the trapping of NPs inside a GAS, indicating that a fraction of NPs is not able to leave the GAS.^[40–42]

To understand the NP growth and transport mentioned above, in situ investigations are necessary. Small-angle X-ray scattering^[40,41] and in situ UV–Vis observations were used to analyze the growth and transport inside the GAS.^[42] These studies reported that

NPs become trapped in the close vicinity of the magnetron due to a complicated interplay between different forces (Figure S1). However, this contradicts the simple theory of NPs linearly growing alongside their paths through the GAS.

In this study, the ongoing processes inside the GAS and the origin of the trapping of NPs inside the GAS are studied in more detail. Therefore, the influence of different Ar flows on the transport and growth of NPs are investigated in situ using UV–Vis spectroscopy. While in recent works the main attention was focused on investigations of trapping at a specific gas flow and pressure,^[40–42] in this study, the impact of different geometrical parameters and gas flows on the trapping behavior inside the GAS is investigated. In particular, this study focuses on the aspects of NP growth and transport in relation to aggregation length and gas flow dynamics.

To determine how the trapping of NPs inside the GAS is influenced by the gas flow, in situ UV–Vis measurements combined with quartz crystal microbalance (QCM) measurements at different magnetron-to-beam distances (M-B distances) are performed (Figure 1). These results are complemented by scanning electron microscopy (SEM) measurements of the synthesized NPs and target surface, profilometer measurements of the target surface, and computational fluid dynamic (CFD) simulations inside the GAS. From these results, we developed a hypothesis on the trapping behavior of NPs in a Haberland-type GAS.

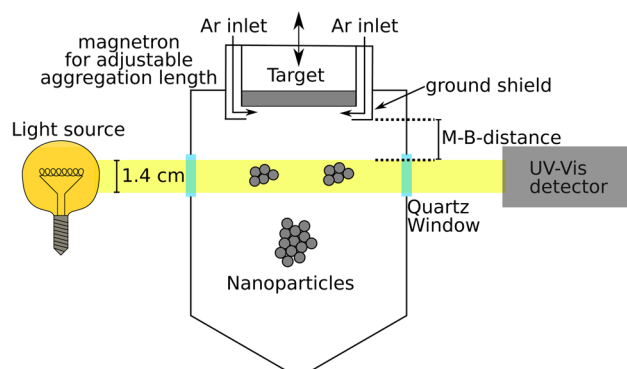


FIGURE 1 Schematic of the experimental setup. The GAS is equipped with a magnetron for adjustable aggregation length. Using this, the M-B distance can be adjusted because the UV–Vis optics is at a fixed position, but the aggregation length of the magnetron can be varied. The light beam of the UV–Vis is 1.4 cm in diameter. The Ar gas inlet is located between the magnetron main body and the ground shield. Hence, the ground shield projects over the magnetron main body, and the Ar gas streams directly over the target surface. GAS, gas aggregation source

2 | EXPERIMENTAL DETAILS

The experiments are performed using a custom-built gas aggregation source equipped with a 2-in. magnetron for adjustable aggregation length (Thin Films Consulting; Ionix) with a 2-in. Ag target (99.99% purity, Kurt J. Lesker). The main vacuum chamber is pumped by a turbo molecular pump (TMU 261, 210 L/s; Pfeiffer) together with a dry scroll vacuum pump (SH-110; Agilent Technologies), and the GAS is connected to the main chamber via an exit orifice (3-mm diameter). The argon gas is injected into the GAS through the magnetron ground shield, allowing for gas delivery directly to the target surface (Figure 1). The flow is controlled using a gas flow controller (1179BX22CM1BV with 200 sccm range; MKS Instruments Deutschland GmbH) and adjusted to 24, 60, 96, and 120 sccm with the corresponding pressures of 49, 113, 177, and 220 Pa inside the GAS. The power supply (MDX 500; Advanced Energy) of the magnetron was operated at 100 W for all experiments. The GAS is equipped with two quartz windows and a UV-Vis spectroscopy setup (Light source: Deuterium/Halogen lamp DH-2000BAL; Detector: Ocean Optics, HR 4000CG-UV-Nir; Ocean Optics). The light beam diameter of the UV-Vis spectroscope is 1.4 cm. To measure the transmission at different M-B distances, the aggregation length was adjusted with the magnetron. The M-B distance of 0 cm corresponds to the closest possible distance between the magnetron and the light beam without cutting the light beam with the ground cap of the magnetron. Since the direct optical emission lines do not contain additional information, these lines were removed to increase the visibility of the plasmonic absorption. As substrates, P-doped, (100)-oriented Si wafer pieces with native oxide (cut to $1 \times 1 \text{ cm}^2$; SiMat) were used. SEM analysis was performed using a Zeiss Ultra Plus microscope.

The flow simulations were conducted using the commercially available software Siemens STAR CCM + 15.04.010 R8. Further details about the CFD simulations can be found in the Supporting Information.

3 | RESULTS AND DISCUSSION

In the first part of the work, the time evolution of the localized surface plasmon resonance (LSPR) of Ag NPs inside the GAS for an Ar flow of 24 sccm and an M-B distance of 3 cm to the target will be exemplarily discussed. In Figure 2a,b, transmittance UV-Vis spectra are shown and presented in two different ways. Figure 2a shows the spectra from 0 to 30 s in 5 s steps as a conventional two-dimensional (2D) plot, where the different

spectra are offset by 5% to increase the visibility of the evolution of the LSPR. The same spectra are also contributing in Figure 2b, where the transmittance is represented by a color bar; on the X-axis, the wavelength is shown, and on the Y-axis, the time is shown. This makes it possible to include all spectra between 0 and 30 s in one plot. With time, the LSPR of the Ag NPs undergoes a strong red shift from ~ 360 to ~ 380 nm, the absorption increases from $\sim 1\%$ to $\sim 9\%$, and also the peak broadens. A red shift together with peak broadening of the LSPR indicates that the NPs are growing over time.^[43,44] In this case, the red shift of the LSPR and the peak broadening are related to the depolarization phenomenon.^[45,46] This observation indicates that the nucleation and growth at the beginning of the NP formation have not reached a stable equilibrium, which is in good agreement with the theory of NP growth inside a GAS.^[32,40–42] After a stable nucleus is formed, it can grow further by condensation of sputtered atoms on the NP surface,^[32] which provides a possible explanation for the observed time evolution in the spectrum.

To estimate the diameter of NPs, extinction cross-sectional area estimations based on the dissertation of Steven J. Oldenburg^[47] are performed. Here, the full vectorial solution to Maxwell's equations is solved without approximation for the problem of light scattering at a homogeneous sphere. The resulting extinction cross-sectional area is a superposition of the absorption cross-sectional area and the scattering cross-sectional area. In this case, only the extinction cross-sectional area is of interest because the UV-Vis measurements only show reduced transmission without differentiation between light scattering and absorption. From these estimations, it turned out that Ag NPs with a diameter of 40 nm have the maximum extinction cross-sectional area at 360 nm, and NPs with a diameter of 70 nm have the maximum extinction cross-sectional area at 380 nm under vacuum conditions and a broader peak (Figure 2c).^[47] The comparison with the UV-Vis data indicates that the NPs in our experiment should have a size of ~ 40 nm in the early growth phase and increase up to ~ 70 nm after ~ 25 s of continuous magnetron operation in GAS. Nevertheless, such large NPs were never observed on the substrate located outside the GAS in front of the orifice. Although the comparison of the UV-Vis data with the estimations in Figure 2c indicates the presence of large NPs up to 70 nm, this does not exclude the presence of smaller NPs because the UV-Vis signal is a superposition of the interaction of the incoming light with several NPs, which may have different sizes. SEM micrographs indicate that the mean diameter of the extracted and deposited NPs is ~ 15 nm and the largest NPs were ~ 35 nm (Figures 2d and S3). This implies that the NPs with diameters larger

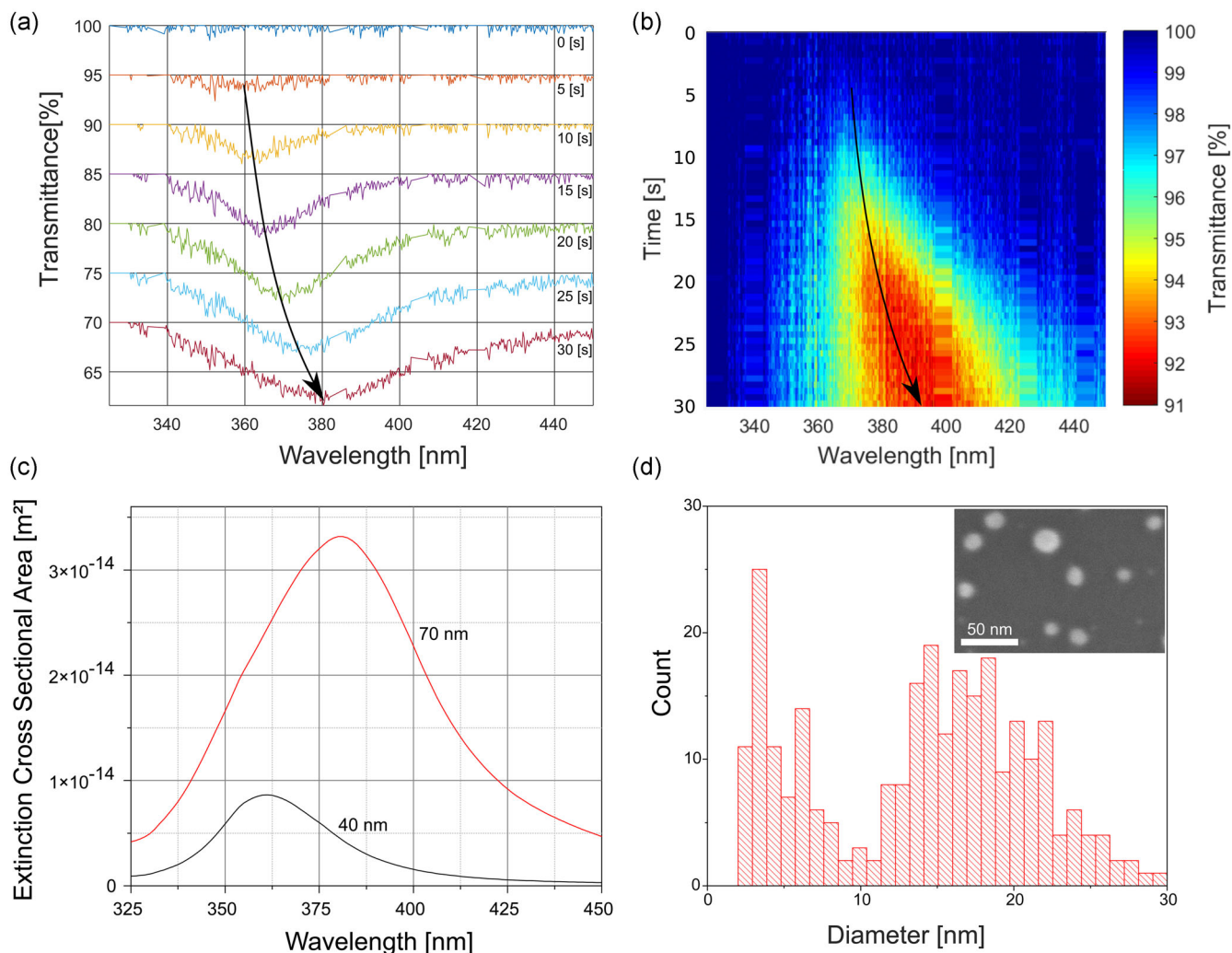


FIGURE 2 UV-Vis spectra showing the time evolution of the LSPR of Ag NPs with a flow of 24 sccm and an M-B distance of 3 cm. The spectra are offset by 5% to increase the visibility of the LSPR. (a) The color map shows the data of (a) together with all other spectra recorded between 0 and 30 s. It can be seen that the LSPR undergoes a red shift over time and the absorption increases, which is related to the growth of NPs and the density of NPs. (b) Estimated extinction cross-sectional areas for NPs with sizes of 40 and 70 nm dependent on the wavelength are shown for comparison with the results of the UV-Vis measurements. (c) The histogram shows the size distribution of NPs deposited on a Si substrate outside the GAS at 24 sccm and an M-B distance of 3 cm. The inset shows an image section of an exemplary SEM image that was considered for the histogram (d). GAS, gas aggregation source; LSPR, localized surface plasmon resonance; NP, nanoparticle; SEM, scanning electron microscopy

than 35 nm, whose presence inside the GAS is predicted based on UV-Vis, can, for some reason, not leave the GAS. Thus, they are either deposited on the inside walls of the GAS apparatus or redeposited onto the target. Considering that the UV-Vis data indicate that large NPs are present in close vicinity to the magnetron, there must be some forces that prevent the NPs from leaving the GAS. Since the UV-Vis light beam passes through the center of the GAS, the NPs would be expected to be transported perfectly by the drag force from the Ar gas outside the GAS. Nevertheless, the phenomenon of large NPs inside GAS that were not able to leave the GAS is known and is referred to as the trapping of NPs.^[40–42]

The observation of an evolving LSPR in the vicinity of the target surface implies that NPs of considerable sizes are formed already close to the target. This is consistent with earlier observations by Kousal et al.^[41] and Shelemin et al.,^[40] who applied synchrotron radiation to perform small-angle X-ray scattering experiments. They found that the NPs grow over time and that large NPs become trapped due to electrostatic force interactions with the charged NPs in close vicinity to the target.

In the second part of this study, NP trapping will be discussed in more detail. To gain an understanding of the location at which the majority of NPs are trapped (i.e., trapping position), the following experiment was

performed: The M-B distance was varied by adjusting the position of the magnetron. In addition, the argon gas flow was varied, which in turn impacted the operating pressure inside the GAS.

Figure 3 shows the UV-Vis spectra for flows of 24 (a) and 60 sccm (b) at different M-B distances at 30 s of magnetron operation. For 24 sccm, it can be clearly seen that the maximum absorption is at an M-B distance of 1 cm. On the other hand, the maximum absorption for a flow of 60 sccm was found at 3 cm. In particular, the observation of a maximum in LSPR in the close vicinity to the target surface is deviating from the common theory of NP growth and transport, which assumes continuous growth of NPs along their transport path.^[32]

Considering that considerable NP growth is already finished in the close vicinity of the target and that the particles do not get lost, the UV-Vis signal must not change when the M-B distance is changed. Assuming that the particles are growing over their whole transport path from the magnetron to the exit orifice, the transmittance in the UV-Vis signal must decrease and the wavelength has to increase. This has to be the case, because with growing size of NPs, the LSPR is red-shifted and broadened, and the extinction cross-sectional area is also increasing (Figure 2c).

This is not the case, and indicates that particles are becoming trapped at different positions, depending on the gas flow and pressure. Accordingly, the common theory of steady nucleation, growth, coalescence, and transport needs to be extended by including the possibility that particles become trapped inside the GAS. In fact, the observations of a maximum in LSPR in the vicinity to the target surface imply that trapping is a highly important component of the overall NP formation process and hence has to be considered in an updated theory.

The data in Figure 3 show that a higher gas flow directly affects the trapping behavior of the NPs in the GAS. The maximum absorption for 24 sccm at an M-B distance of 1 cm is $\sim 24\%$ and that for 60 sccm at an M-B distance of 3 cm is $\sim 6\%$. Since the transmittance is decreased in the same wavelength range, one can assume that the size distributions are also close to each other. This allows the assumption that the absorption is related to the amount of NPs; this means that a significantly smaller amount of NPs becomes trapped with higher gas flows. When the flow is increased to 96 sccm or even up to 120 sccm, almost no absorption due to the LSPR of the Ag NPs can be found (Figure S2). This implies that the higher drag force, which originates from the higher gas flow in combination with higher pressure, can release more of the trapped particles out of the trapping region. This was also proven by QCM measurements (Figure 3c), which have shown an increased deposition rate for increasing flows. The plot shows that for a constant power of 100 W, the deposition rate increases with gas flow from 24 to 120 sccm and is 34 times higher for 120 sccm than for 24 sccm. This indicates that more NPs are released from the GAS, even when the same power was applied to the target.

In a conventional GAS deposition experiment with a fixed exit orifice diameter and pumping rate, any increase in gas flow results in an increase in pressure inside the GAS. This can also change the growth of the NPs. However, the NPs outside the GAS are still in the same diameter range for 60 sccm as for 24 sccm (Figure S3). The fact that the NPs' size distributions for 24 and 60 sccm are close to each other even when the deposition rate for 60 sccm is already reasonably higher than for 24 sccm implies that the increase in drag force is only able to release the smaller NPs out of the "trapping"

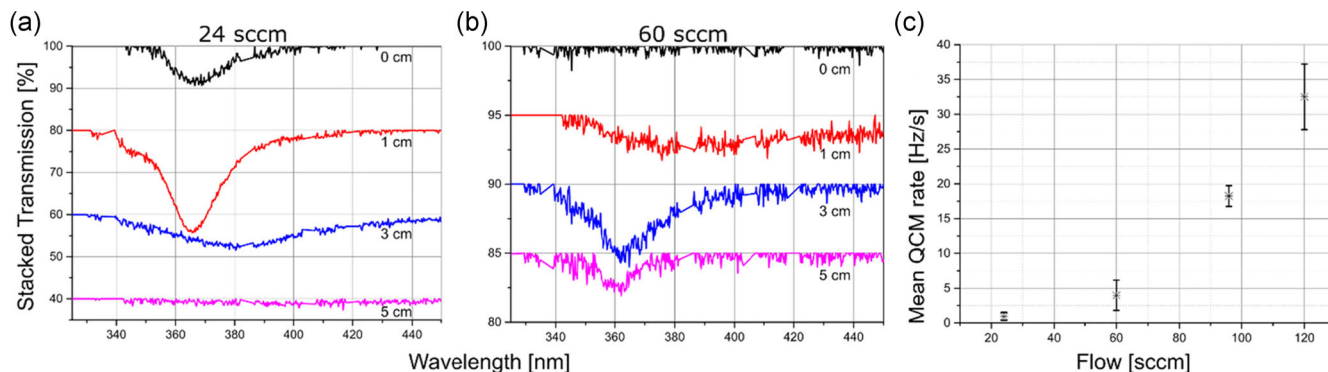


FIGURE 3 UV-Vis spectra at 24 (a) and 60 sccm (b) at different M-B distances after discharge was switched on for 30 s. The spectra have an offset of 20% for 24 sccm and 5% for 60 sccm. It turned out that for 24 sccm, the highest absorption was found 1 cm away from the magnetron, which is referred to as the trapping region. In contrast, the trapping region for 60 sccm was found at 3 cm. Dependence of the deposition rate of Ag NPs on the Ar flow measured with a QCM can be found in (c). Depositions were performed at a constant magnetron power of 100 W. The values are given together with standard deviation error bars. NP, nanoparticle; QCM, quartz crystal microbalance

region because, otherwise, one would expect that also NPs of up to 70 nm or at least 40 nm would be found on the substrate, whose presence was indicated by UV-Vis spectroscopy in the gas phase. To further investigate the "trapping" of NPs and to figure out how big the earlier mentioned forces acting on the NPs are, further research with novel methods has to be conducted. Especially the question why big NPs of up to 70 nm can not escape the GAS but were found with the UV-Vis investigations can only be answered, when the force equilibrium of the NPs is further investigated.

To identify the potential trapping locations inside the GAS, in the third part of the work, CFD simulations were performed using the commercially available software "Siemens STAR CCM+15.04.010 R8." Before discussion of the CFD results, the conditions for trapping or loss of particles have to be defined. In the context of this study, a loss region is indicated by a velocity magnitude of 0 m/s or close to 0 m/s (<0.02 m/s). If an NP is entering a region with a gas velocity close to 0 m/s, the drag force that is forcing the NPs to leave the GAS through the orifice is missing and the NPs will potentially collide with the chamber wall. Therefore, the regions with a gas velocity close to 0 m/s are termed loss regions.

A trapping region is defined as a region with a non-zero velocity and the presence of an additional driving force, which counteracts the drag force and directs the NPs to a stationary trajectory. The NPs in a GAS source can be charged due to the plasma environment and be trapped by a complicated interplay of drag forces from the Ar gas, electromagnetic force, thermophoretic force, gravity, and ion drag force.^[40–42] The forces acting on the NPs are schematically shown in Figure S1.

In Figure 4, the CFD simulation results for 24 sccm at an M-B distance of 0 cm are shown. For all CFD simulations in this study, a linear scale of the velocity was chosen and the range was set from 0 to 0.5 m/s. This was necessary because velocities of up to 100 m/s can be found close to the exit orifice and at the gas inlets. If the linear scale is set to such high values, the visibility of changes in the velocity distribution in the region of interest would be decreased to an unacceptable level. In the Supporting Information, CFD simulations for all flows with a logarithmic scale can be found (Figure S4). Therefore, blue regions are not exactly 0 m/s, but close to 0 m/s, and red regions are 0.5 m/s or higher, which can be seen in Figure S4. Using UV-Vis spectroscopy as a diagnostic approach to determine the NP trapping region, the area under investigation is limited to the beam trajectory of the UV-Vis light source. For a better comparison, the region corresponding to the UV-Vis light beam is also indicated as a yellow bar in the visualization of the CFD simulation. In Figure 4, three different

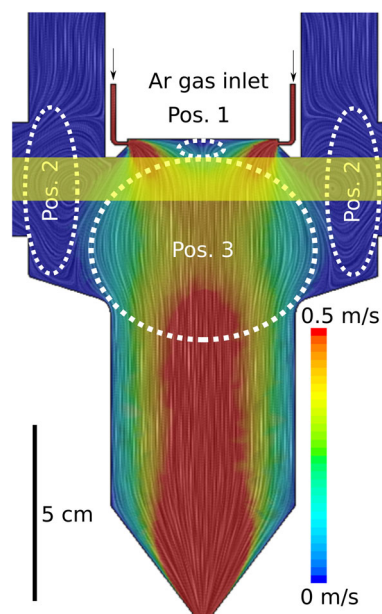


FIGURE 4 An exemplary CFD velocity distribution is shown. Here, the yellow region corresponds to the position of the UV-Vis light beam at an M-B distance 0 cm. Three different positions (Pos.) are shown. Positions 1 and 2 correspond to loss regions and Position 3 corresponds to the trapping region. The flow direction of the gas is indicated by white stream lines. The gas inlet is shown and located between the ground cap and the magnetron. CFD, computational fluid dynamic

positions in the gas stream are shown. Position 1 and Position 2 are loss regions where the velocity magnitude equals nearly 0 m/s (blue regions). To distinguish Position 1 and Position 2 more easily, they are termed the "proximal loss region" (PLR), which is close to the target, and the "distal loss region" (DLR), which is further away from the target. Position 3 indicates the possible trapping region. In the next section, first, the possible PLR and DLR, where the gas velocity is close to 0 m/s, will be discussed.

The PLR is directly in front of the target in the center position and the DLR is left and right from the mainstream of the gas when we depict the GAS in a 2D representation. In a 3D representation, the DLR can be described by a torus with its rotational symmetry axis aligned to the rotational symmetry axis of the target. It is expected that NPs can get lost at both loss regions. The loss of NPs from the PLR region is indicated by the Profilometer and SEM measurements. The profile and the SEM images at the center of the target, which is close to the PLR region, show clearly that material was redeposited there (Figure 5). A profile of $0\ \mu\text{m}$ corresponds to the original target surface height before any deposition was carried out. It is clear that, everywhere, material is redeposited onto the target surface, except at the erosion

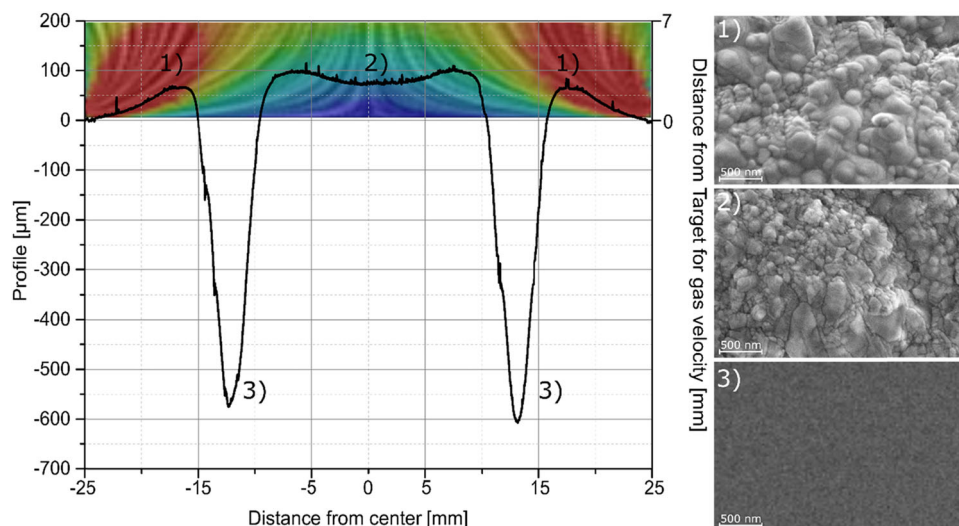


FIGURE 5 Profilometer measurements after target usage and corresponding SEM pictures at different places of the target. CFD velocity distribution above the target is inserted into the profilometer measurement plot. The CFD section shows ~ 7 mm of the velocity distribution above the target. The color bar is identical to Figures 4 and 6 and ranges from 0 (blue) to 0.5 m/s (red). The profile shows less redeposition at the low-velocity region (blue) than at the high-velocity region (red). CFD, computational fluid dynamic; SEM, scanning electron microscopy

zone. The phenomenon of redeposition in GAS sources has been reported many times and is much more pronounced in comparison to conventional thin-film sputter deposition with magnetrons.^[40,42,48] The profile shows that much more material is redeposited onto the center (max. height: ~ 100 nm) of the target than onto the sides of the target (max. height: ~ 67 nm).

The SEM images at the redeposition regions show that the redeposited material consists of NPs but also single atoms can contribute to the redeposition. On the contrary, the SEM micrographs from the erosion zone show a smooth surface, as expected for a sputtered surface. In particular, the increase in the redeposition from the outer edge of the target toward the onset of the erosion zone indicates a strong effect of the gas flow on the redeposition behavior. The CFD simulations have shown that the gas velocity is high at the sides of the target because the gas inlet is located there. On the other hand, the velocity in front of the center of the target is 0 m/s. The profilometer measurements together with the CFD simulations indicate that NPs that are formed in the close vicinity of the target sides are guided into the main Ar gas flow, which prevents redeposition. If the NPs are close to the middle of the target, a considerably higher amount of NPs becomes redeposited in comparison to the sides of the target. The low-velocity area close to the target, despite being mostly shadowed by the ground cap of the magnetron, can still contribute to the UV-Vis spectra of the PLR in the visible region.

The PLR would be visible in the UV-Vis spectra at an M-B distance of 0 cm even when a part of the PLR is

shadowed by the ground cap. This means that for 60 sccm, definitely no particles were found in the visible region for this possible trapping because at an M-B distance of 0 cm, no absorption is visible (Figure 3). On the other hand, for 24 sccm at an M-B distance of 0 cm, absorption was present, which means that NPs are present at that M-B distance. Since the UV-Vis measurement technique obtains data from the cylindrical volume at a specific M-B distance, one obtains information only from the volume and not from specific positions in space. In case of a gas flow of 24 sccm at an M-B distance of 0 cm, the UV-Vis measurement includes the PLR, DLR, and trapping region. The observation of absorption in the corresponding UV-Vis measurement indicates the presence of NPs in either of the PLR, DLR, or trapping regions.

At the DLR, no samples could be placed; therefore, no SEM or profilometer measurements were possible. Nevertheless, after the deposition experiments, the entirety of the inside walls of the GAS showed NP deposits, which proves that NPs are sometimes deposited on walls in loss regions (Figure S5). However, according to the theory of the working principle of a GAS, particles are transported out of the GAS only because of the gas flow. From this point of view, particles can get lost potentially at the PLR and also at the DLR.

In the following section, the influence of changes in the gas flow and the M-B distance on the Ar gas velocity is discussed. Therefore, CFD simulations for 24 and 60 sccm and M-B distances of 0, 1, and 3 cm were conducted, and these are shown in Figure 6. In this figure,

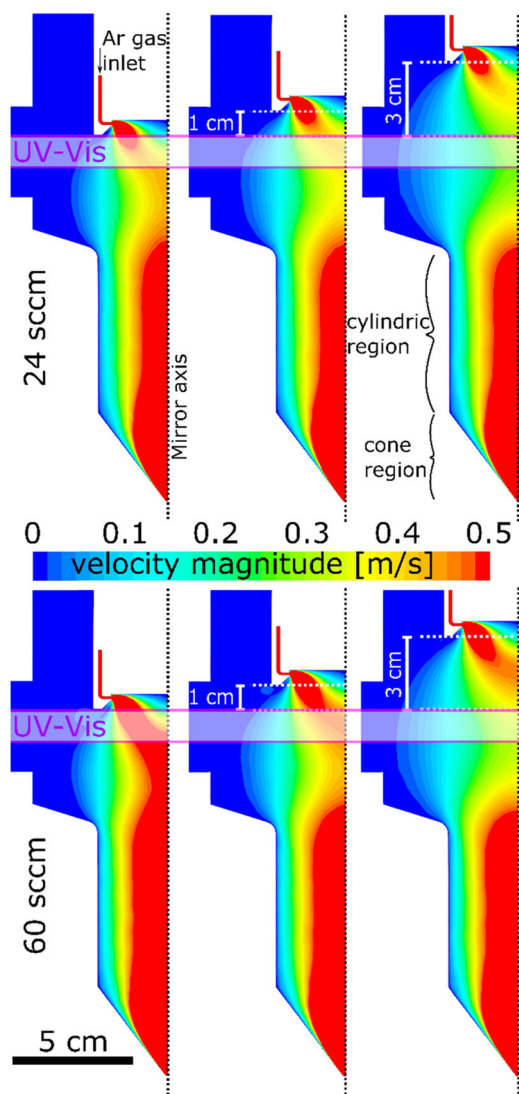


FIGURE 6 CFD flow simulation for 24 (top) and 60 sccm (bottom) and for different M-B distances of 0, 1, and 3 cm from left to right. The black dotted line indicates the mirror axis. The violet beam locates the position and the size of the UV-Vis light beam. The loss regions (blue) are not much affected by changes in gas flow or the M-B distance. An increase in the M-B distance leads to an increase in the low-velocity region in the center of the GAS. On the other hand, an increase in gas flow leads to an increase in the gas velocity everywhere but does not affect the shape of the flow. CFD, computational fluid dynamic; GAS, gas aggregation cluster source

the color code shows the velocity magnitude of the Ar gas atoms inside the GAS, which is restricted to the range 0–0.5 m/s. The borders of the colored regions correspond to the inside walls of the GAS. In total, six different simulations are shown. Each row corresponds to one Ar flow (24 sccm on top and 60 sccm at the bottom) and the resulting pressure (49 and 113 Pa), and each column corresponds to an M-B distance, which is shown in white color. In each GAS simulation, the magnetron is located

on the top and the exit orifice is located on the bottom. The schematic depiction of the UV-Vis light beam indicates the approximate volume from which the UV-Vis spectra are originating. These simulations showed three different behaviors depending on the changed parameters and the regions of interest, which will be described and discussed in the following section (Figures 4 and 6):

- 1) The velocity distributions in the PLR and DLR are not much affected by the change in the gas flow or the changes in the aggregation length. The UV-Vis spectra show that the M-B distance where the particles are trapped changes depending on the gas flow (Figure 3). This indicates that the NPs most probably do not get lost only in the 0 m/s velocity regions (PLR and DLR) inside the GAS because these regions are almost not affected by the change of gas flow. From this point of view, it follows that there must exist a trapping region in the higher velocity regions in the mainstream of the Ar gas inside the GAS as described earlier.
- 2) The trapping region, which is located inside the mainstream of the Ar gas stream, has shown more differences. With an increase in gas flow, the velocity in the center of the GAS is also increasing. This increase, together with the increase of the pressure, increases the drag force on the NPs drastically. Experimentally, this is related to the increased NP deposition rate from Figure 3c found already and is also reflected by the change of the trapping position from 1 cm for 24 sccm to 3 cm for 60 sccm (Figure 3a,b).
- 3) A change in the aggregation length affects the velocity distribution in the trapping region. It turned out that the region close to the magnetron, the cylindrical region, and the cone region (Figure 6) in the GAS remained nearly unaffected. However, the region between the magnetron and the cylindrical region of the GAS with lower velocities is increasing. On this basis, on the one hand, the NPs are transported better at higher gas flows and pressures because they are guided better into the mainstream of Ar by the increased drag force. On the other hand, for lower flows, the drag force is too low to overcome the other forces that are trapping the NPs. However, the UV-Vis results indicated that large NPs are present inside the GAS, but it is unclear why they cannot be deposited onto the substrate. Most probably, the forces related to the plasma, which are trapping the NPs, are higher for larger NPs and cannot be overcome by higher gas flows or they cannot follow the gas stream as good as the small ones, due to their higher mass. More investigations on this topic are needed in the future.

Here, in situ UV-Vis spectroscopy can be an important analytical tool to expand the understanding of trapping and transport.

With the increase in the M-B distance, the aggregation length was also increased, which also slightly increased the size of the resulting NPs (Figure S3). The mean NP size increases with the M-B distance from ~ 12 to ~ 17 nm for 24 sccm and from ~ 12 to ~ 16 nm for 60 sccm. The CFD simulations showed that with an increase in the aggregation length, not only was the aggregation region increased but also the gas flow was affected. Accordingly, the residence time of the NPs was not only increased because the aggregation zone was increased but also because the gas velocity and therefore the velocity of NP that were not trapped were decreased, which in turn increased the time for the growth of the NPs. The size distributions also showed that a bimodal distribution is much more pronounced with higher gas flow, pressure, and aggregation length. The simulations showed that the diversity in the velocity distribution in the GAS increases with an increase in aggregation length and increase in the gas flow. This may be the reason for the resulting bimodal distributions because the NPs, depending on their path through the GAS, can have very different conditions for growth and transport. The bigger population in the size distribution, which is the group of NPs around the second maximum in the size distribution, can also be a result of coalescence between several NPs of the smaller population. This may be much more probable for the higher gas flows because the deposition rate was much higher and so the probability for coalescence is higher. On the other hand, it has to be pointed out that the actual geometry of the GAS, as well as the magnetron, is of crucial importance. While some magnetrons have a gas inlet between the ground shield and the target, as shown here, others have a gas inlet at a certain place behind the magnetron. Although these instrumental details have not received much attention yet, we want to point out that even small differences in different GAS setups can cause huge differences in the gas flow.

On combining the UV-Vis results, profilometer measurements, and CFD simulation, it was found that forces other than the drag force influence the NPs during their growth and transport because otherwise, no particle trapping would be observed in the trapping region. In addition, the CFD simulations showed that the velocity in the aggregation zone decreased with increasing aggregation length, which increased the residence time of NPs in the GAS in addition to the longer path.

The results indicate that an updated theory for the growth and transport of NPs is urgently required. With a

better understanding of NP growth and transport processes, especially taking the trapping mechanism into account, it would be possible to tailor the sizes of NPs more efficiently. We were able to show that the gas flow and its velocity distribution have a huge impact on the transport of NPs, which should be considered as a more important parameter in the design of future GAS sources. Already during the construction process, CFD simulations can be performed and special attention should be paid to the appearance of low-velocity regions. These regions can be, in some circumstances, useful to tune the size of NPs, if a means for the release of these NPs can also be found. Also, the gas inlet location should be considered as a critical construction part to reduce re-deposition onto the target.

4 | CONCLUSION

In this study, gas flow-related transport phenomena in GAS have been studied and two indications for trapping of NPs are observed. On the one hand, in situ UV-Vis spectroscopy found evidence of a time-dependent red shift and broadening of the LSPR peak, which can be seen as an indication of NP growth. Comparing UV-Vis data to estimated extinction cross sections for differently sized NPs, larger particles are expected to be trapped inside the GAS than those observed in the deposit. By means of UV-Vis measurements and the magnetron for adjustable aggregation length, it has been found that the position of the trapping region inside the GAS can be significantly influenced by different gas flows and pressures.

On the other hand, CFD simulations were conducted to determine the working gas flow pattern. The CFD simulations have shown that the gas flow in the loss regions does not differ much. Therefore, their position is always nearly the same with varying gas flows and pressures. However, the velocity distribution of the gas inside the possible trapping region changed considerably with different aggregation lengths and gas flows. In addition, the velocity distribution close to the target revealed that a loss region (PLR) is present there. This has been confirmed by profilometer measurements (more NP material is redeposited in the center of the target in comparison to the outer side of the target).

Finally, in conclusion, the gas velocity pattern determines, to a huge extent, the transport of NPs inside the GAS and therefore it should be treated as a crucial parameter in the designing process of future gas aggregation cluster sources. This may lead to considerably increased production rates of NPs and thus constitute an important milestone for industrial applications.

ACKNOWLEDGMENTS

This study was financially supported by the German Research Foundation (DFG) via the project PO2299/1-1. The authors would like to thank Stefan Rehders for technical assistance. Special thanks are due to Siemens's official distributor in the Czech Republic, TechSim s.r.o., for providing the license for the CFD software Siemens STAR CCM+.

CONFLICT OF INTERESTS

The authors declare that there are no conflict of interests.

AUTHOR CONTRIBUTIONS

Jonas Drewes, Alexander Vahl, Oleksandr Polonskyi, Thomas Strunskus, and Franz Faupel developed the idea and conceived the initial design of the study. Jonas Drewes, Oleksandr Polonskyi, and Alexander Vahl established the experimental setup. Jonas Drewes performed the Ag NP depositions and recorded UV-Vis data. Jonas Drewes, Alexander Vahl, and Oleksandr Polonskyi analyzed the results. Suren Ali performed the computational fluid dynamic simulations. Jonas Drewes and Alexander Vahl prepared the manuscript draft. Alexander Vahl and Franz Faupel supervised the work of Jonas Drewes. Hynek Biederman supervised the work of Suren Ali. All authors discussed the experimental results and their analysis and revised and approved the manuscript.


DATA AVAILABILITY STATEMENT

The UV-Vis spectra and scanning electron microscopy pictures that support the findings of this study are available from the corresponding author upon reasonable request.

ORCID

Jonas Drewes  <http://orcid.org/0000-0002-8539-1543>

Suren Ali-Ogly  <http://orcid.org/0000-0002-2808-8353>

Thomas Strunskus  <http://orcid.org/0000-0003-3931-5635>

Oleksandr Polonskyi  <http://orcid.org/0000-0001-5013-0944>

Hynek Biederman  <http://orcid.org/0000-0003-4061-8481>

Franz Faupel  <https://orcid.org/0000-0003-3367-1655>

Alexander Vahl  <http://orcid.org/0000-0002-7311-272X>

REFERENCES

- [1] D. Astruc, *Chem. Rev.* **2020**, *120*, 461.
- [2] M. Z. Ghorji, J. Adam, O. C. Aktas, S. Veziroglu, B. B. Shurtleff, T. Strunskus, F. Faupel, O. Polonskyi, A. Hinz, *ACS Appl. Nano Mater.* **2018**, *1*, 3760.
- [3] S. Veziroglu, M. Z. Ghorji, A. L. Obermann, K. Röder, O. Polonskyi, T. Strunskus, F. Faupel, O. C. Aktas, *Phys. Status Solidi A* **2019**, *216*, 1.
- [4] S. Veziroglu, J. Hwang, J. Drewes, I. Barg, J. Shondo, T. Strunskus, O. Polonskyi, F. Faupel, O. C. Aktas, *Mater. Today Chem.* **2020**, *16*, 100251.
- [5] A. Vahl, S. Veziroglu, B. Henkel, T. Strunskus, O. Polonskyi, O. C. Aktas, F. Faupel, *Materials* **2019**, *12*, 2840.
- [6] H. Li, Z. Li, Y. Yu, Y. Ma, W. Yang, F. Wang, X. Yin, X. Wang, *J. Phys. Chem. C* **2017**, *121*, 12071.
- [7] C. Minnai, M. Di Vece, P. Milani, *Nanotechnology* **2017**, *28*, 0.
- [8] C. Minnai, A. Bellacicca, S. A. Brown, P. Milani, *Sci. Rep.* **2017**, *7*, 1.
- [9] M. Mirigliano, D. Decastri, A. Pullia, D. Dellasega, A. Casu, A. Falqui, P. Milani, *Nanotechnology* **2020**, *31*, 234001.
- [10] M. Mirigliano, F. Borghi, A. Podestà, A. Antidormi, L. Colombo, P. Milani, *Nanoscale Adv.* **2019**, *1*, 3119.
- [11] Z. Wang, S. Joshi, S. E. Savel'ev, H. Jiang, R. Midya, P. Lin, M. Hu, N. Ge, J. P. Strachan, Z. Li, Q. Wu, M. Barnell, G. L. Li, H. L. Xin, R. S. Williams, Q. Xia, J. J. Yang, *Nat. Mater.* **2017**, *16*, 101.
- [12] H. Jiang, D. Belkin, S. E. Savel'Ev, S. Lin, Z. Wang, Y. Li, S. Joshi, R. Midya, C. Li, M. Rao, M. Barnell, Q. Wu, J. J. Yang, Q. Xia, *Nat. Commun.* **2017**, *8*, 882.
- [13] B. J. Choi, A. C. Torrezan, K. J. Norris, F. Miao, J. P. Strachan, M. X. Zhang, D. A. A. Ohlberg, N. P. Kobayashi, J. J. Yang, R. S. Williams, *Nano Lett.* **2013**, *13*, 3213.
- [14] S. H. Jo, T. Chang, I. Ebong, B. B. Bhadviya, P. Mazumder, W. Lu, *Nano Lett.* **2010**, *10*, 1297.
- [15] X. B. Yan, J. H. Zhao, S. Liu, Z. Y. Zhou, Q. Liu, J. S. Chen, X. Y. Liu, *Adv. Funct. Mater.* **2018**, *28*, 1.
- [16] V. Postica, A. Vahl, D. Santos-Carballal, T. Dankwort, L. Kienle, M. Hoppe, A. Cadi-Essadek, N. H. De Leeuw, M. I. Terasa, R. Adelung, F. Faupel, O. Lupan, *ACS Appl. Mater. Interfaces* **2019**, *11*, 31452.
- [17] Y. Yong, C. Li, X. Li, T. Li, H. Cui, S. Lv, *J. Phys. Chem. C* **2015**, *119*, 7534.
- [18] S. W. Choi, A. Katoch, G. J. Sun, S. S. Kim, *Sens. Actuators, B* **2013**, *181*, 446.
- [19] F. Fan, J. Zhang, J. Li, N. Zhang, R. R. Hong, X. Deng, P. Tang, D. Li, *Sens. Actuators, B* **2017**, *241*, 895.
- [20] K. Hassan, G. S. Chung, *Sens. Actuators, B* **2017**, *239*, 824.
- [21] S. Enoch, B. Nicolas, A. Adibi, T. W. Hänsch, F. Krausz, B. A. J. Monemar, H. Venghaus, H. Weber, H. Weinfurter, in *Plasmonics* (Eds: S. Enoch, N. Bonod), Springer, Berlin, Heidelberg **2012**.
- [22] P. Anger, P. Bharadwaj, L. Novotny, *Phys. Rev. Lett.* **2006**, *96*, 3.
- [23] H. A. Atwater, A. Polman, *Nat. Mater.* **2010**, *9*, 865.
- [24] H. X. Xu, E. J. Bjerneld, M. Käll, L. Börjesson, *Phys. Rev. Lett.* **1999**, *83*, 4357.
- [25] P. Cherukuri, E. S. Glazer, S. A. Curley, *Adv. Drug Delivery Rev.* **2010**, *62*, 339.
- [26] V. Zaporozhchenko, R. Podschun, U. Schürmann, A. Kulkarni, F. Faupel, *Nanotechnology* **2006**, *17*, 4904.
- [27] X.-F. Zhang, Z.-G. Liu, W. Shen, S. Gurunathan, *Int. J. Mol. Sci.* **2016**, *17*, 1534.
- [28] W. de Heer, *Rev. Mod. Phys.* **1993**, *65*, 611.
- [29] V. N. Popok, E. E. B. Campbell, *Rev. Adv. Mater. Sci.* **2006**, *11*, 19.
- [30] K. Wegner, P. Piseri, H. V. Tafreshi, P. Milani, *J. Phys. D: Appl. Phys.* **2006**, *39*, R439.
- [31] H. Haberland, M. Karrais, M. Mall, Y. Thurner, *J. Vac. Sci. Technol., A* **1992**, *10*, 3266.

- [32] Y. Huttel, *Gas-Phase Synthesis of Nanoparticles*, Wiley-VCH Verlag GmbH & Co. KGaA, Weinheim, Germany **2017**.
- [33] M. Gracia-Pinilla, E. Martínez, G. S. Vidaurri, E. Pérez-Tijerina, *Nanoscale Res. Lett.* **2010**, *5*, 180.
- [34] T. Hihara, K. Sumiyama, *J. Appl. Phys.* **1998**, *84*, 5270.
- [35] S. Pratontep, S. J. Carroll, C. Xirouchaki, M. Streun, R. E. Palmer, *Rev. Sci. Instrum.* **2005**, *76*, 045103.
- [36] M. Hillenkamp, G. Di Domenicantonio, C. Flix, *Rev. Sci. Instrum.* **2006**, *77*, 025104.
- [37] H. Haberland, M. Mall, M. Moseler, Y. Qiang, T. Reiners, Y. Thurner, *J. Vac. Sci. Technol., A* **1994**, *12*, 2925.
- [38] J. Bai, J. P. Wang, *Appl. Phys. Lett.* **2005**, *87*, 1.
- [39] I. Shyjumon, M. Gopinadhan, C. A. Helm, B. M. Smirnov, R. Hippler, *Thin Solid Films* **2006**, *500*, 41.
- [40] A. Shelemin, P. Pleskunov, J. Kousal, J. Drewes, J. Hanuš, S. Ali-Ogly, D. Nikitin, P. Solař, J. Kratochvíl, M. Vaidulych, M. Schwartzkopf, O. Kylián, O. Polonskyi, T. Strunskus, F. Faupel, S. V. Roth, H. Biederman, A. Choukourov, *Part. Part. Syst. Charact.* **2020**, *37*, 1.
- [41] J. Kousal, A. Shelemin, M. Schwartzkopf, O. Polonskyi, J. Hanuš, P. Solař, M. Vaidulych, D. Nikitin, P. Pleskunov, Z. Krtouš, T. Strunskus, F. Faupel, S. V. Roth, H. Biederman, A. Choukourov, *Nanoscale* **2018**, *10*, 18275.
- [42] D. Nikitin, J. Hanuš, S. Ali-Ogly, O. Polonskyi, J. Drewes, F. Faupel, H. Biederman, A. Choukourov, *Plasma Processes Polym.* **2019**, *16*, 1.
- [43] G. Xu, M. Tazawa, P. Jin, S. Nakao, *Appl. Phys. A: Mater. Sci. Process.* **2005**, *80*, 1535.
- [44] J. J. Mock, M. Barbic, D. R. Smith, D. A. Schultz, S. Schultz, *J. Chem. Phys.* **2002**, *116*, 6755.
- [45] M. Meier, A. Wokaun, *Opt. Lett.* **1983**, *8*, 581.
- [46] P. W. Barber, R. K. Chang, H. Massoudi, *Phys. Rev. Lett.* **1983**, *50*, 997.
- [47] S. J. Oldenburg, *Light Scattering from Gold Nanoshells*, Rice University, Houston, TX, USA **2000**.
- [48] J. Drewes, A. Vahl, N. Carstens, T. Strunskus, O. Polonskyi, F. Faupel, *Plasma Processes Polym.* **2020**, *1*.

SUPPORTING INFORMATION

Additional supporting information may be found in the online version of the article at the publisher's website.

How to cite this article: J. Drewes, S. Ali-Ogly, T. Strunskus, O. Polonskyi, H. Biederman, F. Faupel, A. Vahl. Impact of argon flow and pressure on the trapping behavior of nanoparticles inside a gas aggregation source. *Plasma Processes Polym.* **2022**;19:e2100125.
<https://doi.org/10.1002/ppap.202100125>